Rev. Roum. Sci. Techn.– Électrotechn. et Énerg.
Vol. **69**, *2*, pp. 153–158, Bucarest, 2024

A DECOUPLED MAGNETIC INTEGRATION TECHNIQUE FOR DUAL-FREQUENCY TOPOLOGIES

SHENGWEI GAO[1], YONGXIAO LI[1], HAOBO ZHANG[1], JINRUI TIAN[1]

Keywords: Dual frequency dc/dc converter; Magnetic integration; Power density; Three-section winding; Finite element simulation.

The dual-frequency converter comprises a high-frequency buck unit and a low-frequency buck unit, which has the advantages of high efficiency and fast dynamic response. But also, the increase of magnetic parts leads to the power density of the converter being greatly reduced; for this problem, this paper proposes a three-section winding method to decouple the two inductors in the converter integrated into a magnetic core, given the integrated magnetic parts structure and establish its gyrator-capacitor model to derive the decoupling conditions. The flux density distribution of the magnetic components is analyzed by finite element simulation software and compared with the existing integration method; this decoupling integration method can make the flux distribution more uniform and improve the core utilization. The results show that the volume and weight are reduced by 31.2 % and 25.3 % compared with those of the separated magnetic parts, and the efficiency is also consistent with that of the separated magnetic parts, which verifies the correctness and feasibility of the theoretical analysis.

1. INTRODUCTION

With the relentless advancements in power electronics technology, high frequency has emerged as a dominant theme within the electronics industry. However, operating at high frequencies can lead to a surge in converter switching losses, which ultimately impedes the converter's efficiency [1–4]. According to the literature [5], a special converter, the dual-frequency buck converter (DF Buck), is proposed, which can improve the converter response speed while reducing the switching losses and improving the converter efficiency. This topology comprises a high-frequency Buck converter and a low-frequency buck converter. The high-frequency Buck converter is primarily responsible for accelerating the system's dynamic response speed, while the inductor on the low-frequency Buck flows through the high-frequency inductor on the current shunt, thereby reducing switching losses and enhancing system efficiency. Literature [6–11] primarily focuses on the parametric design principles of DF Buck, the power transfer path, and the development of a small signal model. These studies demonstrate that the output characteristics of DF Buck are mainly dependent on high-frequency parameters and remain independent of low-frequency parameters. Although DF Buck successfully addresses the conflicting relationship between individual high frequency and output efficiency, it also increases the size and weight of the converter due to the addition of a large low-frequency inductor in the topology. This increase in size and weight leads to higher costs and limited operating environments.

To tackle this issue, researchers have studied the magnetic elements of DF Buck and increasingly utilized magnetic integration techniques [12] to reduce the size and weight of magnetic components. For instance, in literature [13], the coupling integration principle is employed to integrate the input inductor, two power transfer inductors, and one auxiliary inductor into a single core, resulting in a “zero” output current ripple and achieving better dynamic performance. Similarly, in [14], a high-gain integrated inductor method is proposed to vary the conversion rate of coupled inductors, which improves voltage gain while simultaneously reducing the pulse of the output current. Additionally, [15] proposes a decoupled magnetic integration method for DF Buck. However, this integral structure may lead to the saturation of side columns and an uneven flux density distribution. Conversely, literature [16] on LLC resonant converters integrates the resonant inductor and transformer into the core, which reduces the leakage inductance between transformer windings and mitigates the magnetic saturation problem of the integrated magnetic components.

We propose a new integration method to address the issues of volume and weight of magnetic components in DF Buck and the existing integration method [15] that results in easy saturation of core side columns. This method involves dividing the low-frequency large inductor into three sections and winding them on each core column. Meanwhile, the high-frequency small inductor is wound on the middle column of the core, and the decoupling condition is derived by using the gyrator-capacitor model. The proposed integration method effectively reduces the size and weight of the core, resulting in a more uniform flux density distribution, higher core utilization, and better shunt effect. To verify the accuracy of our theory, we utilize finite element simulation software and an experimental prototype to compare the separate magnetic (SM), existing integrated magnetic (IM), and three-section winding integrated magnetic (TSWIM) methods.

2. INTEGRATION METHOD AND CORE SELECTION

As shown in Fig. 1a), to ensure a more uniform flux density distribution throughout the core of the TSWIM, we propose winding and integrating the magnetic parts in the following manner. First, the low-frequency large inductor is divided into three sections and wound on the two side columns and the lower half of the middle column. The high-frequency small inductor is wound on the upper half of the middle column. This setup utilizes several low-frequency and high-frequency inductors wound on different magnetic columns, each with their respective number of turns. The number of turns of the low-frequency inductor L_{L1} wound on magnetic column I is denoted by N_{11}, while N_{12} and N_{13} represent the number of turns of L_{L2} and L_{L3} wound on magnetic columns III and II, respectively. The total number of turns of the low-frequency inductors is given by $L_L = L_{L1}$

[1] School of Electrical Engineering and Automation, Tiangong University, No. 399 BinShuiXi Road, XiQing District, Tianjin 300387, P.R. of China.
Emails: gaoshengwei@tiangong.edu.cn, lxsyforever.163.com, zhanghaobo688@163.com, 15866356857@sina.cn

DOI: 10.59277/RRST-EE.2024.69.2.6

+ L_{L2} + L_{L3}. Additionally, N_{22} indicates the number of turns of the high-frequency inductor L_H wound on magnetic column III. The flux generated by L_H is denoted by Φ_{22}, while Φ_{11}, Φ_{12}, and Φ_{13} represent the fluxes generated by low-frequency inductors L_{11}, L_{12}, and L_{13}. Finally, U_H and U_L are the voltages across the high-frequency and low-frequency inductors, respectively, while i_H and i_L represent the corresponding currents. The IM magnetic structure is shown in Fig. 1b), as described in the literature [15].

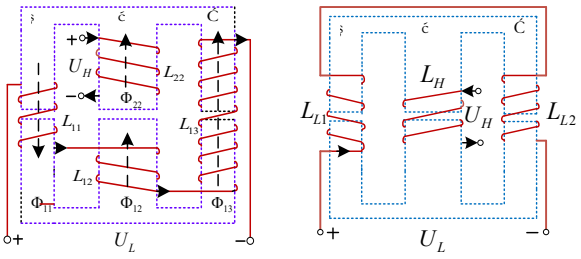

Fig. 1 – Magnet structure; a) TSWIM; b) IM.

Drawing from the literature [17], we develop the gyrator-capacitor model of the TSWIM, where C_I, C_{II}, and C_{III} denote the equivalent permeabilities on the corresponding magnetic columns, respectively (as depicted in Figure 2). In Fig. 3, we see the air gap and cross-sectional area of the TSWIM, wherein la is the core air gap size, and A_I, A_{II}, and A_{III} represent the core cross-sectional area size. For EE cores, it is common practice to take the cross-sectional area of the center column as twice the cross-sectional area of the side columns for ease of analysis; thus, we have $2A_I = 2A_{II} = A_{III}$. Furthermore, μ_0 denotes vacuum magnetic permeability.

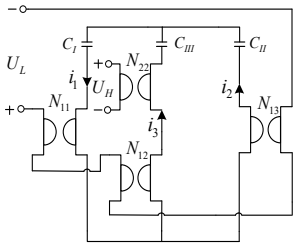

Fig. 2 – Gyrator-capacitor model of TSWIM.

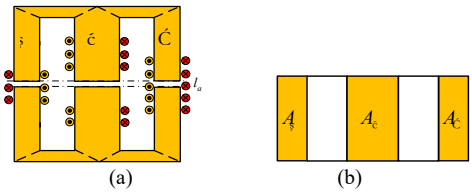

Fig. 3 – Cross-sectional area and air gap of TSWIM: a) air gap; b) core cross-sectional area

Figure 2 reveals that when the current is not induced into the high-frequency winding on the middle column of the core, we can observe that:

$$i_3(s)=i_1(s)\frac{C_{III}}{C_{II}+C_{III}}-i_2(s)\frac{C_{III}}{C_I+C_{III}}+\frac{N_{12}i_L}{\frac{1}{sC_{III}}+\frac{1}{sC_I}//\frac{1}{sC_{II}}}, \quad (1)$$

where:

$$i_1(s)=\frac{N_{11}i_L}{\frac{1}{sC_I}+\frac{1}{sC_{II}}//\frac{1}{sC_{III}}}, \quad (2)$$

$$i_2(s)=\frac{N_{13}i_L}{\frac{1}{sC_{II}}+\frac{1}{sC_I}//\frac{1}{sC_{III}}}, \quad (3)$$

$$C_I=\frac{\mu_0 A_I}{l_a},\ C_{II}=\frac{\mu_0 A_{II}}{l_a},\ C_{III}=\frac{\mu_0 A_{III}}{l_a}, \quad (4)$$

If the current i_3 running through the high-frequency winding on the middle column is zero, there will be no interaction between the high-frequency and low-frequency windings. By substituting eq. (2) and eq. (3) into eq. (1), we can obtain:

$$N_{11}i_L C_I C_{III}-N_{13}i_L C_{II}C_{III}+N_{12}i_L C_{III}(C_I+C_{II})=0\,. \quad (5)$$

Simplifying eq. (5) yields

$$N_{11}+2N_{12}-N_{13}=0\,. \quad (6)$$

Suppose current is added solely to the high-frequency winding, and no current is added to the low-frequency winding.

$$i_1(s)=i_3(s)\frac{C_I}{C_I+C_{II}}, \quad (7)$$

$$i_2(s)=-i_3(s)\frac{C_{II}}{C_I+C_{II}}, \quad (8)$$

$$U_L(s)=i_1(s)N_{11}+i_2(s)N_{13}+i_3(s)N_{12}\,. \quad (9)$$

Substituting eq. (7) and (8) into eq. (9), we get:

$$U_L(s)=i_1(s)N_{11}+i_2(s)N_{13}+i_3(s)N_{12}\,. \quad (10)$$

If $U_L(s) = 0$, the voltage coupled by the high-frequency winding on the low-frequency winding will be zero. In this scenario, eq. (10) can be simplified to:

$$N_{11}+2N_{12}-N_{13}=0\,. \quad (11)$$

When the design parameters of the low-frequency winding satisfy eq. (11), both high and low-frequency inductors can achieve the decoupling integration. From Fig. 2, the high and low-frequency inductance size can be calculated as:

$$L_H=N_{22}^2[(C_I+C_{II})//C_{III}], \quad (12)$$

$$L_L=(N_{11}+N_{12}+N_{13})^2[C_I//(C_{II}+C_{III})]\,. \quad (13)$$

To ensure the core's column saturation is considered, two steps should be followed before selecting a core. First, calculate the maximum flux each column may pass through to determine whether it is in saturation or at the saturation boundary. Secondly, an appropriate window area should be ensured to accommodate the windings. The equivalent magnetic circuit of TSWIM can be drawn from Fig. 1(a), as shown in Fig. 4.

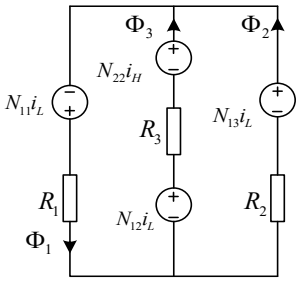

Fig. 4 – Equivalent magnetic circuit model of TSWIM

The magnetic resistances equivalent to those on magnetic columns I, II, and III are represented by R_1, R_2, and R_3, respectively, in Fig. 4. The magnetic fluxes on magnetic columns I, II, and III are indicated by Φ_1, Φ_2, and Φ_3. Further,

low-frequency inductors L_{L1}, L_{L2}, and L_{L3} generate magnetic potentials $N_{11}i_L$, $N_{12}i_L$, and $N_{13}i_L$, respectively, while high-frequency inductor L_H generates magnetic potential $N_{22}i_H$.

Based on Ohm's law of the magnetic circuit, the maximum magnetic induction generated on each magnetic column can be determined using the following equation:

$$\Delta B_{\mathrm{I,max}}=\frac{L_{\mathrm{L1}}i_{L,\max}}{N_{11}A_{\mathrm{I}}}, \tag{14}$$

$$\Delta B_{\mathrm{II,max}}=\frac{L_{\mathrm{L3}}i_{L,\max}}{N_{13}A_{\mathrm{II}}}, \tag{15}$$

$$\Delta B_{\mathrm{III,max}}=\frac{L_H i_{H,\max}}{N_{22}A_{\mathrm{III}}}+\frac{L_{\mathrm{L2}}i_{L,\max}}{N_{12}A_{\mathrm{III}}}. \tag{16}$$

The minimum flux densities they produce are:

$$\Delta B_{\mathrm{I,min}}=\frac{L_{\mathrm{L1}}i_{L,\min}}{N_{11}A_{\mathrm{I}}}, \tag{17}$$

$$\Delta B_{\mathrm{II,min}}=\frac{L_{\mathrm{L3}}i_{L,\min}}{N_{13}A_{\mathrm{II}}}, \tag{18}$$

$$\Delta B_{\mathrm{III,min}}=\frac{L_H i_{H,\min}}{N_{22}A_{\mathrm{III}}}+\frac{L_{\mathrm{L2}}i_{L,\min}}{N_{12}A_{\mathrm{III}}}. \tag{19}$$

Expressed using the superposition theorem, the absolute value of the maximum flux density on each column can be determined as follows:

$$B_{\mathrm{I,max}}=\Delta B_{\mathrm{I,max}}+\frac{1}{2}\Delta B_{\mathrm{II,max}}+\frac{1}{3}\Delta B_{\mathrm{III,max}}, \tag{20}$$

$$B_{\mathrm{II,max}}=\Delta B_{\mathrm{II,max}}+\frac{1}{3}\Delta B_{\mathrm{I,max}}-\frac{1}{2}\Delta B_{\mathrm{III,min}}, \tag{20}$$

$$B_{\mathrm{III,max}}=\Delta B_{\mathrm{III,max}}+\frac{2}{3}\Delta B_{\mathrm{I,max}}-\frac{2}{3}\Delta B_{\mathrm{II,min}}. \tag{22}$$

The maximum and minimum flux densities on magnetic columns I, II, and III are represented by $\Delta B_{\mathrm{I,max}}$ /$\Delta B_{\mathrm{I,min}}$, $\Delta B_{\mathrm{II,max}}$ /$\Delta B_{\mathrm{II,min}}$, and $\Delta B_{\mathrm{III,\,max}}$ /$\Delta B_{\mathrm{III,\,min}}$, respectively, in the above equations. Additionally, $i_{H,\mathrm{max}}$/$i_{H,\ \mathrm{min}}$ and $i_{L,\mathrm{max}}$/$i_{L,\mathrm{min}}$ represent the peak and valley values of the high-frequency and low-frequency inductance currents, respectively. We can judge whether the selected magnetic core has local saturation through the above equation.

The core's window area must be met to ensure integrated components function properly.

$$A_W \geq \max\{\frac{N_{11}d_{11}+N_{11}d_{11}}{K_{Cu}},\frac{N_{22}d_{22}+N_{13}d_{13}}{K_{Cu}}\}. \tag{23}$$

The equation for determining the required window area (A_W) for integrated components involves using the corresponding winding wire diameters (d_{11}, d_{12}, and d_{13}) and the copper fill factor (K_{Cu}).

3. MAGNETICALLY INTEGRATED DF BUCK MODAL ANALYSIS

Figure 5 shows the DF buck under SM and the DF buck under TSWIM, respectively, where Q_1 to Q_4 are switching tubes. Q_1 and Q_4 are high-frequency switches, while Q_2 and Q_3 are low-frequency switches. The low-frequency inductor divides the current on the high-frequency inductor to minimize switching losses and improve efficiency. Based on the literature [11], the switching states can be categorized into four states, as presented in Table 1. The corresponding modal transitions are illustrated in Fig. 6. Additionally, the theoretical output waveform of the DF Buck can be observed in Fig. 7. Since the modalities of SM, TSWIM, and IM are the same, only the modal analysis of TSWIM is carried out.

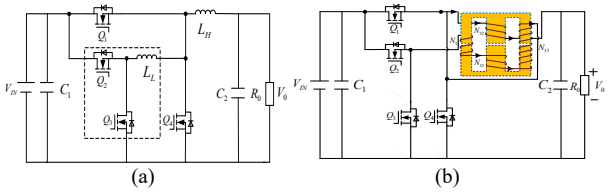

Fig. 5 – DF Buck converter: a) SM DF Buck; b) TSWIM DF Buck.

Table 1
Four switching states

Mode	Switching action			
	Q_1	Q_2	Q_3	Q_4
(1)	ON	ON	OFF	OFF
(2)	OFF	ON	OFF	ON
(3)	ON	OFF	ON	OFF
(4)	OFF	OFF	ON	ON

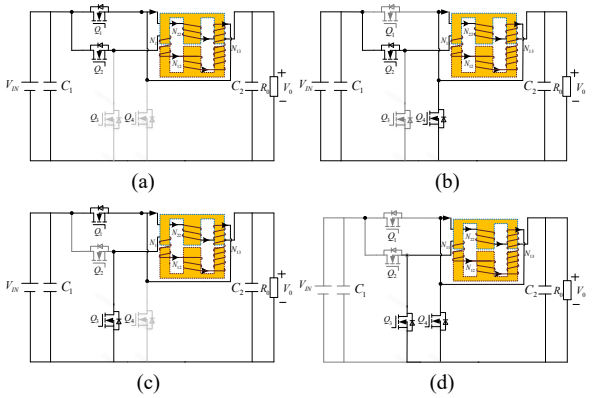

Fig. 6– Four modes of DF Buck: a) Mode 1; b) Mode 2; c) Mode 3; d) Mode 4

The equation of state can be expressed as when the converter is in mode (a):

$$\begin{bmatrix}\frac{di_H}{dt}\\ \frac{di_L}{dt}\end{bmatrix}=\begin{bmatrix}\frac{U_H}{L_H}\\ \frac{U_L}{L_L}\end{bmatrix}=\begin{bmatrix}\frac{V_{in}-V_0}{L_H}\\ 0\end{bmatrix}. \tag{24}$$

In this mode, the voltage across L_H is positive, while the voltage across L_L is zero. The current i_H increases linearly while the inductor current i_L remains constant during this time.

The equation of state can be expressed as when the converter is in mode (b):

$$\begin{bmatrix}\frac{di_H}{dt}\\ \frac{di_L}{dt}\end{bmatrix}=\begin{bmatrix}\frac{U_H}{L_H}\\ \frac{U_L}{L_L}\end{bmatrix}=\begin{bmatrix}\frac{-V_0}{L_H}\\ \frac{V_{in}}{L_L}\end{bmatrix}. \tag{25}$$

During this mode, the voltage across L_H becomes negative, causing the current i_H to decrease. At the same time, the voltage across L_L is positive, resulting in a gradual increase of the inductor current i_L.

The equation of state can be expressed as when the converter is in mode (c):

$$\begin{bmatrix}\frac{di_H}{dt}\\ \frac{di_L}{dt}\end{bmatrix}=\begin{bmatrix}\frac{U_H}{L_H}\\ \frac{U_L}{L_L}\end{bmatrix}=\begin{bmatrix}\frac{V_{in}-V_0}{L_H}\\ \frac{-V_{in}}{L_L}\end{bmatrix}. \tag{26}$$

When in this mode, the voltage across L_H is positive, causing an increase in current i_H. Conversely, the voltage across L_L is negative, leading to a decrease in the inductor current i_L.

The equation of state can be expressed as when the

converter is in mode (d):

$$\begin{bmatrix} \frac{di_H}{dt} \\ \frac{di_L}{dt} \end{bmatrix} = \begin{bmatrix} \frac{U_H}{L_H} \\ \frac{U_L}{L_L} \end{bmatrix} = \begin{bmatrix} \frac{-V_0}{L_H} \\ 0 \end{bmatrix} . \quad (27)$$

In this mode, the voltage across L_H becomes negative, causing the current i_H to start falling. Meanwhile, the voltage across L_L is zero, resulting in a constant current flow i_L that does not change.

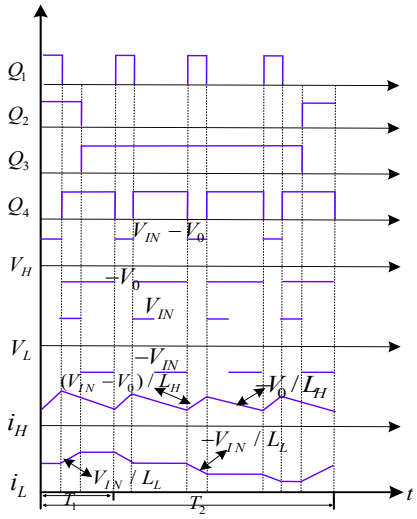

Fig. 7 – The waveform of TSWIM DF Buck.

4. SIMULATION OF MAGNETICALLY INTEGRATED DF BUCK

The gyrator-capacitor model is a suitable approach to establishing the relationship between electricity and magnetism in simulations, which is why it is commonly used in circuit and magnetic circuit simulations. By transforming the TSWIM into a gyrator-capacitor model, the two inductors in the DF Buck can be substituted with the gyrator-capacitor model and integrated into the overall circuit. The control method utilized in this context involves regulating the average current. Figure 8 illustrates the co-simulation topology, while Table 2 outlines the simulation parameters.

Table 2
Simulation parameters.

Parameters	Value
Input voltage V_{IN}	48V
Output voltage V_0	12V
Filter Capacitor C_1/C_2	300μF
High-frequency inductorsL_H	50μH
Low-frequency inductors L_L	200μH
Resistance R_0	1.33Ω
High-frequency switching frequency f_H	200kHz
Low-frequency switching frequency f_L	50kHz

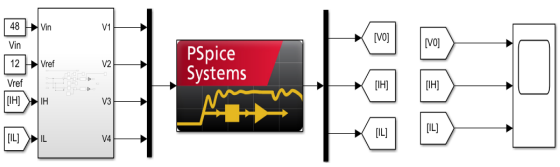

Fig. 8 – Co-simulation circuit of TSWIM DF Buck.

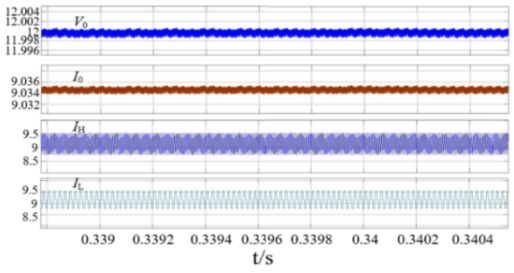

Fig. 9 – Steady-state waveform of TSWIM DF Buck.

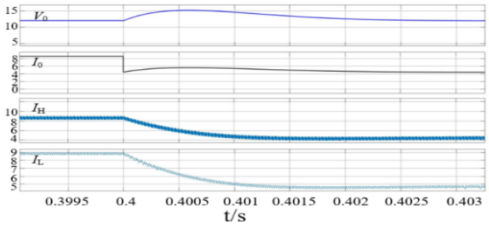

Fig. 10 – Load jump waveform of TSWIM DF Buck.

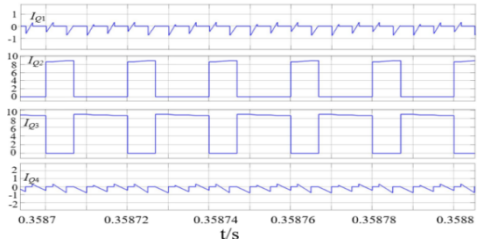

Fig. 11 – Current flowing through each switching device.

The waveforms simulated by adding the equivalent integrated magnetic part TSWIM constructed using the gyrator-capacitor model to the DF BUCK are shown in Figs. 9-11. Figure 9 shows the steady state waveforms, which shows that the output voltage is stabilized at 12 V, the voltage ripple magnitude is 4mV, and the high-frequency inductor current ripple and the low-frequency inductor current ripple are about 1 A, which is following the theoretically calculated values. To test the dynamic response speed of the converter, it is tested for load jumping, and it can be seen from Fig. 10 that the output voltage has about 3V overshoot when the load R_0 is changed to 0.5 R_0, and then it returns to the stable state after 2ms. Figure 11 shows the current flow of each switching device in the converter. It can be seen that the current flow on the high-frequency switches Q_1 and Q_4 is very small, and the current flow on the low-frequency switches Q_2 and Q_3 is very large. This is because the low-frequency unit takes the current from the high-frequency unit, and this can be used to reduce the switching losses, which is the most important characteristic of the DF Buck.

5. FINITE ELEMENT SIMULATION OF MAGNETIC PARTS

To compare the flux density distribution of SM, IM, and TSWIM, finite element simulations are performed for each of the three, and the inductance size is kept consistent with the simulation. The core is a PC95 ferrite core with a saturation flux density BM of about 0.35 T. The selection of magnetic cores is realized according to the AP method. In [18], the selection rules are as follows:

$$\Delta B_m = B_m \cdot \frac{\Delta I_m}{I_{sp}} , \quad (28)$$

$$AP=\left[\frac{L\cdot I_{sp}}{B_M}\cdot\frac{I_{FL}}{K_1}\right]^{\frac{4}{3}} . \quad (29)$$

Determine the number of winding turns:

$$N=\frac{L\cdot\Delta I_m}{\Delta B_m\cdot A_e} . \quad (30)$$

Determination of core air gap:

$$l=\frac{\mu_0 N^2 A_e}{L} . \quad (31)$$

In the above equation, ΔB_m is the maximum flux swing, ΔI_m is the inductor current ripple value, L is the value of the inductor, I_{SP} is the maximum short-circuit current, I_{FL} is the effective value of the inductor current at full load, and K_1 is the single-coil inductance coefficient, A_e is the effective cross-sectional area of the magnetic core. the finite element simulation results are as follows:

Table 3

Parameters of IM.

Core type	Inductance Type	Number of turns	Air gap
EE42	High-frequency inductance	24	1.2 mm
	Low-frequency inductance	34	

Table 4

Parameters of TWSIM.

Core type	Inductance Type	Number of turns	Air gap
EE42	High-frequencyinductanceN_{22}	17	1.2 mm
	Low-frequencyinductanceN_{11}	12	
	Low-frequencyinductanceN_{12}	12	
	Low-frequencyinductanceN_{13}	36	

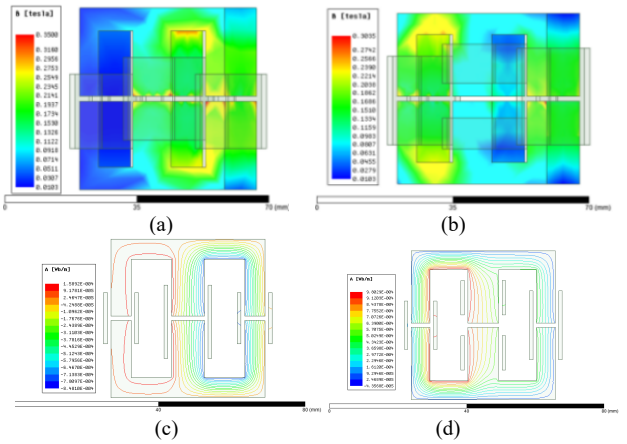

Fig. 12 –Full load finite element simulation: a) IM; b) TSWIM; c) IM magnetic line distribution; d) TSWIM magnetic line distribution.

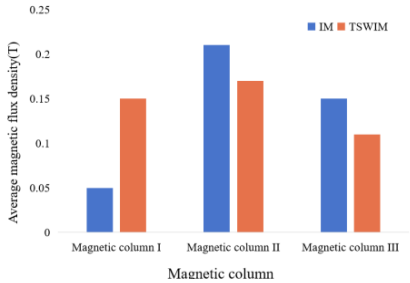

Fig. 13 – Average magnetic flux density of each column of the integrated magnetic part.

Figure 12 shows the finite element simulations of IM and TSWIM with the same excitation applied, respectively, and it can be seen that the flux density distribution of TSWIM is significantly better than that of IM, and the flux density of IM is mainly concentrated in columns II and III, while the flux density distribution of TSWIM is relatively homogeneous, which can also be derived from the distribution of the magnetic lines of force of IM and TSWIM. Figure 13 shows a schematic diagram comparing the magnitude of the average magnetic flux density of IM and TSWIM.

6. EXPERIMENT

A 108W DF Buck experimental platform was established in Figure 14 to confirm the validity of the previous analysis and derivation. Table 5 shows the equipment, switching devices, and models used in the experiment. To compare magnetic parts, separate experimental verification was conducted on SM, IM, and TSWIM, with all parameters remaining constant except for the converter's magnetic component, which had been substituted. The experimental parameters align with those of the simulation, and the outcomes are presented as follows. Figure 15 shows a comparison of the three magnetic parts.

Table 5

Equipment and model used for experiments.

Equipment	Brands	Model
Oscilloscope	Tektronix	MD03014
Voltage probe	Tektronix	TPP0200
Current Probe	Tektronix	TCP0030A
DC Power Supply	Aviatec	IPP3000P
Auxiliary power	RIGOL	DP832
Electronic load	ITECH	IT8514B
Switching Devices	Infineon	IRF640

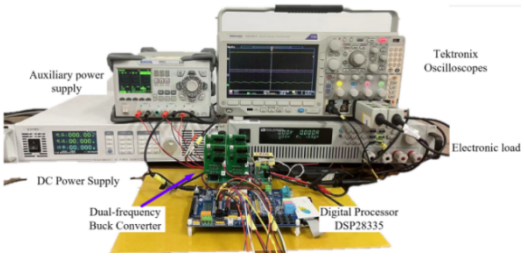

Fig. 14 – Experimental platform.

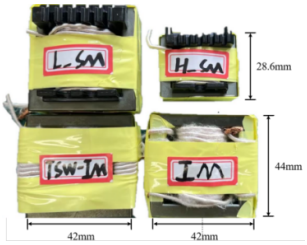

Fig. 15 – Comparison of magnetic parts.

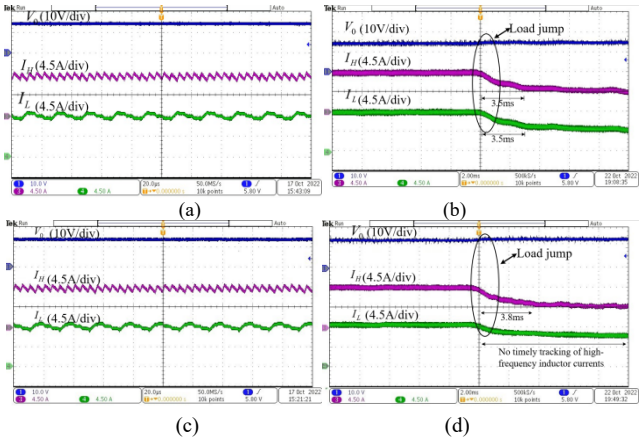

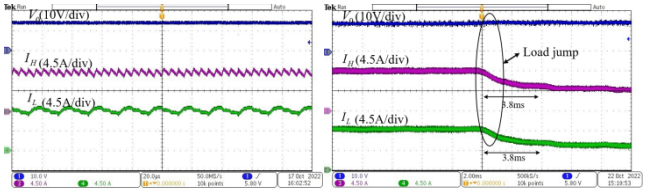

(e) (f)

Fig. 16 –Experimental waveform; a) Steady-state waveform of SM; b) Load jump waveform of SM; c) Steady-state waveform of IM; d) Load jump waveform of IM; e) Steady-state waveform of TSWIM; f) Load jump waveform of TSWIM.

Figure 16 depicts the steady-state waveforms of the SM, IM, and TSWIM for the DF Buck, respectively. The results show that all three magnetic components enable stable converter operation. Load hopping experiments were conducted to assess the dynamic response speed of the converter with the three magnetic elements. The findings indicate that TSWIM has the closest and almost synchronous dynamic response speed with SM, while IM exhibits a slower response rate and inferior shunt effect compared to TSWIM. Hence, TSWIM performs similarly to SM in terms of dynamic performance while ensuring the steady operation of the converter. Figure 17 illustrates the overall efficiency of the experimental prototype. The efficiency comparison demonstrates that TSWIM's efficiency is comparable to SM's, thereby validating the theoretical analysis.

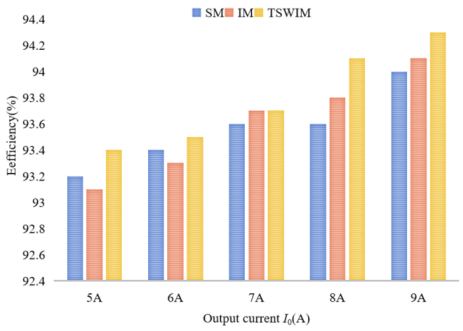

Fig. 15 – Efficiency comparison.

7. CONCLUSIONS

This paper proposes a novel technique for integrating magnetic components in a dual-frequency Buck converter using a three-section winding approach. By adopting this integration method, the conventional separated magnetic parts can be replaced, reducing the size and weight of the system's magnetic components by 31.2 % and 25.3 %, respectively. Consequently, the power density of the system improves. Compared to existing integration methods, TSWIM offers higher core utilization, more uniform magnetic density distribution, and superior shunt effect of shunt cells. To validate the theoretical analysis, an experimental prototype with a rating of 108 W was constructed and tested, demonstrating the correctness and reliability of the proposed approach.

Received on 27 August 2023

REFERENCES

1. G. Hua, F.C. Lee, *Soft-switching techniques in PWM converters*, IEEE Transactions on Industrial Electronics, **42**, 6, pp. 595–603 (1995).
2. X.G. Yang, D.X. Wang, Z. Jia, *Load and input voltage adaptive zero-voltage soft-switching full-bridge converter*, Trans. China Electrotech., **37**,12, pp. 3061–3072 (2022).
3. S.A.Q. Mohammed, J.W. Jung, *A state-of-the-art review on soft-switching techniques for dc-dc, dc-ac, ac-dc, ac-ac power converters*, IEEE Transactions on Industrial Informatics, **17**, 10, pp. 6569–6582 (2021).
4. C. Fei, F.C. Lee, Q. Li, *High-Efficiency High-Power-Density LLC Converter with an Integrated Planar Matrix Transformer for High-Output Current Applications*, IEEE Transactions on Industrial Electronics, **64**, 11, pp. 9072–9082 (2017).
5. L.W. Zhou, X. Du, Z.H. Fu, *Dual frequency buck converter*, Proc. CESS, **26**, 6, pp. 68–72 (2006).
6. X. Du, L.W. Zhou, Q.M. Luo, *Effect of dual frequency buck converter parameters on system performance*, Trans. China Electrotech., **20**, 11, pp. 49–55 (2005).
7. Q.M. Luo, L.W. Zhou, W.G. Luo, *Performance analysis and design of dual frequency Buck converter*, Trans. China Electrotech., **23**, 5, pp. 56–61 (2008).
8. Q.M. Luo, L.W. Zhou, W.G. Luo, *Operating mode of dual frequency buck converter*, Trans. China Electrotech., **23**, 11, pp. 72-78 (2008).
9. Q.M. Luo, L.W. Zhou, W.G. Luo, *Composite dual frequency buck converter*, Proc. CESS, **28**, 9, pp. 1–6 (2008).
10. X. Du, L. Zhou, H.M. Tai, *Dual frequency Buck converter*, IEEE Transactions on Industrial Electronics, **56**, 5, pp. 1690-1698 (2009).
11. K. Fang, L. Zhou, Q. Liu, *A review of dual frequency transformation theory in converters*, Power System Technology, **34**, 11, pp.135–139 (2010).
12. Q.H. Chen, X.B. Ruan, Y.G. Yan, *Magnetic integration technology and its application in switching power supplies*, Trans., China Electrotech., **19**, 3, pp. 1–18 (2004)
13. H. Zhu, D. Zhang, Y. Zhou, *Integrated magnetic buck-boost converter with "zero" output current ripple*, IEEE Transactions on Industrial Electronics, **68**, 7, pp. 5821–5832 (2021).
14. H.Z. Li, F.Y. Liu, Y. Liu, *A new magnetically integrated high-gain coupled inductor multiplier boost converter*, Trans. China Electrotech., **32**, S2, pp. 450–460 (2020).
15. X.F. Zhamg, L.W. Zhou, Q.W. Luo, *Magnetically integrated dual-band dc-dc converters*, Trans. China Electrotech., **25**, 1, pp.77–83 (2010).
16. S.W. Gao, Z.Y. Zhao, *Magnetic integrated LLC resonant converter based on independent inductance winding*, IEEE Access, **9**, pp.660–672 (2021).
17. Y. Liang, B. Lehman, *A capacitor modeling method for integrated magnetic components in dc/dc converters*, IEEE Transactions on Power Electronics, **20**, 5, pp. 987–996 (2005).
18. J.M. Zhou, X.K. Zhao, *Theory and design of magnetic component of switching power supply*, Bei Hang University Press (2014).
19. Z. Yan, Z. Weibo, T. Guanghui, *A core loss calculation method for dc/dc power converters based on sinusoidal losses*, IEEE Transactions on Industrial Electronics, **38**, 1, pp. 692–702 (2022).